Mechanical Engineering Faculty Scholarship

Mechanical Engineering

8-2017

Parametric Resonance of a Repulsive Force MEMS Electrostatic Mirror

Mehmet Ozdogan
Binghamton University--SUNY

Meysam Daeichin
Binghamton University--SUNY

Abdallah H. Ramini
Gannon University

Shahrzad Towfighian
Binghamton University--SUNY, stowfigh@binghamton.edu

Recommended Citation

Parametric Resonance of a Repulsive Force MEMS Electrostatic Mirror

Mehmet Ozdogan[a], Meysam Daeichin[a], Abdallah Ramini[b], Shahrzad Towfighian[a,*]

[a]*State University of New York at Binghamton, Binghamton, New York 13902*
[b]*Gannon University, 109 University Square, Erie, PA 16501, USA*

Abstract

We investigate the nonlinear dynamic behavior of an electrostatic MEMS mirror. The MEMS mirror is driven by repulsive force actuators, which avoid pull-in instability and enable large travel ranges. In parallel-plate actuators, the force on the structure is toward the substrate limiting the range of motion to the capacitor gap. Unlike parallel-plate, repulsive force actuators push the mirror away from the substrate not limiting the motion. The highly nonlinear nature of the repulsive force and the large motions create unique characteristics that differ from parallel-plate actuators. Repulsive force actuators show linear natural frequency hardening with increased DC voltages unlike parallel-plate ones that have frequency softening. A large parametric resonance is another attribute of repulsive force actuators as the limitations of a small gap and pull-in instability are eliminated. To simulate the system response, we use a lumped parameter model with linear and cubic stiffness modulated by the excitation voltage that causes parametric resonances. Using the shooting technique, we obtained simulations that agree well with the nonlinear responses observed in our experiments. As the limitation of a small gap is overcome, the electrostatic force triggers large principal parametric resonances with amplitudes as large as the primary resonance. The parametric resonance is more pronounced at low DC excitation levels when geometric nonlinearities are not significant (axial stress is low). While the initial gap is only 2 microns, under parametric resonance, our one-millimeter diameter mirror reaches ± 43 μm at 1.2 KHz when the excitation level is as low as $V_{DC} = 40$ V, $V_{AC} = 1$ V in a vacuum. The ability to achieve parametric resonances with repulsive force actuation can serve and improve the signal-to-noise ratio and speed in various applications such as confocal microscopy.

Keywords: MEMS mirror, Repulsive Force, Hardening Behavior, Nonlinear Dynamics

1. Introduction

Micro-electromechanical systems (MEMS) enabled creating high performance miniaturized optical devices such as spectrometers [1] to measure and detect gases and confocal micro-endoscopes [2–4] to obtain high-resolution imaging. Other bio-medical and aerospace applications include optical coherence tomography [5, 6], spatial light modulators [7, 8], adaptive optic applications [9–11], auto-focus camera systems [12, 13], telescopes [9, 11] and laser-based communications [14]. The main component of these measurement devices is a MEMS mirror used for optical path modulation. Among different actuation mechanisms for micro-mirrors including electrothermal,

---

electromagnetic, piezoelectric and electrostatic [15–17], the latter is the most popular because of its fast speed, low power consumption, ease of fabrication and small size. These interesting features of electrostatic micro-mirrors are now used in widespread industrial applications. However, there are two main limitations on electrostatic actuation to obtain a large stroke. First, pull-in instability hampers parallel-plate configurations and comb-drive devices. Second, the devices require a high voltage.

Researchers have devised methods to extend the travel range of the actuators by using levers [14], pantograph suspensions [10], soft polymers [18] and control-based approaches, including current and charge control [19, 20]. The lever-bending approach increases travel range by applying the electrostatic force only to a part of the actuator [21]. However, this method requires high voltages that are not desirable. In another design, Chan et al. [22] added a series of capacitors to keep the electrostatic force constant by controlling the applied voltage. This method again requires high input voltage.

Pull-in occurs when the mechanical restoring force is no longer able to overcome the electrostatic force, which leads to a collapse of the microstructure causing a stiction problem or permanent damage to the microstructure. Several designs have been proposed to reduce the pull-in possibility [23–26]. Among different designs, repulsive electrostatic force configuration is superior to others, because it not only eliminates the pull-in occurrence but also it enables a large out-of-plane motion at lower voltages. That means, it does not restrict the motion of the microstructure to the vertical gap, which is usually a few microns [27]. This large travel range is achieved by pushing the microstructure away from the substrate by using the fringe-field electrostatic force.

The repulsive force scheme was first proposed in 1992 by Tang et al. [28] for comb-drive levitation. Using the asymmetry of an electrostatic field, Lee et al. [29] created a repulsive force for lateral motion. In 2005, He and Ben Mrad [27] presented a MEMS out-of-plane actuator using the repulsive force concept and derived an analytical expression for the repulsive force using the conformal mapping technique.

Despite several studies on static characterization of repulsive force actuators [30, 31], there is a lack of knowledge about the complicated dynamic behavior of these devices arising from the repulsive force. The repulsive force is highly nonlinear, which affects the performance and signal-to-noise ratio of operating devices. Unlike the parallel-plate actuators where the formulation of the electrostatic force is straightforward, the expression for repulsive force is far more complicated. This nonlinear repulsive force triggers nonlinear responses that require further investigations.

This study provides a thorough experimental and analytical investigation of the nonlinear dynamic behavior of a MEMS mirror with repulsive force actuation. Building upon our knowledge from micro-beams, we present an analytical lumped parameter model and verify our simulations with experimental results. The unique property of the repulsive mechanism allows large motions that lead to combined nonlinearities from geometry and the electrostatic force. We report several interesting nonlinear characteristics such as frequency hardening, secondary resonances as well as parametric resonances, that have never been reported for micro-mirrors driven by the repulsive force.

Comparable nonlinear dynamic behaviors of electrostatic actuators such as frequency softening and secondary resonances have been reported for MEMS parallel-plate electrodes [32–34] and micromirrors [35–37]. More attractive than other nonlinear responses, parametric resonances that

2

occur at twice the natural frequency have caused special interest because of the large distinctive responses that can improve sensing, filtering and actuation [38–44]. Low damping environments and the modulation of stiffness by the electrostatic force increase the possibility of parametric resonances. There are several examples of MEMS mirrors driven by parametric resonances such as comb drive microscanners [44], Fourier-transformed infrared spectrometers [1] and confocal microscopes [45, 46]. In this study, we present a one millimeter diameter mirror that shows parametric resonance with $\pm32\,\mu m$ piston motion at 1.2 KHz when DC voltage is 40 V and AC voltage is 1 V. Such low voltage operation and a large range of motion are useful features for confocal microscopy. Our study reveals a better understanding of the parametric resonance of repulsive force actuators and helps in designing higher performance devices with larger signal-to-noise ratios and resolutions.

The paper is organized as follows: Section 2 describes the operating principle. Section 3 presents the experimental setup and discusses results. Mathematical modeling and the system identification are elaborated in Section 4, followed by a conclusion in Section 5.

2. Principle of Operation

The system consists of a MEMS mirror plate surrounded by four sets of circular repulsive force actuators attached to middle beams (Figure 1 (b)). The middle beam is attached to the mirror plate through converting springs and the movable finger on the edge is anchored to the substrate through anchoring springs. Each unit of the actuator consists of a movable finger above three fixed electrodes on a substrate (Figure 1 (e)). This configuration was introduced by He et al. [16, 27] to produce a repulsive force that pushes the moveable finger out of plane. The movable and center electrodes are grounded, while the side electrodes have voltages. This arrangement creates an asymmetric electric field forcing the movable finger to move to an equilibrium point away from the substrate (Figure 2a). The location of this equilibrium point is directly above the center electrode at a distance highly dependent on the geometry of the electrodes. If the movable finger is placed at a distance smaller than the equilibrium point, it will experience a net force away from the electrodes. Otherwise, it will be attracted toward the substrate. With the dimensions we have chosen, this equilibrium point is at 30 microns (Figure 2b). As it is shown in Figure 2c, for the distances above the equilibrium point, the net force is downward (attractive) and for the distances below the equilibrium point, the net force is upward (repulsive).

Upon applying the same voltage difference to four sets of actuators, the repulsive force makes the actuators rotate along rotation axes. This rotational behavior is converted to translational motion of the mirror using converting springs (Figure 1 (d)). Compared to a previous design [30], which used a square area for the actuators, here we used a circular area with circumferential fingers. Using circumferential fingers in our new design not only reduces the form factor, but also increases the length of fingers (the longest finger from $836\mu m$ to $1094\mu m$) in the same area. This increase leads to a larger repulsive force and hence a larger displacement at a specific voltage.

3. Experimental Results and Discussion

The actuator system is made of polysilicon and is fabricated through a PolyMUMPS standard commercial fabrication process [47]. The mirror and actuator dimensions are listed in Table 1.
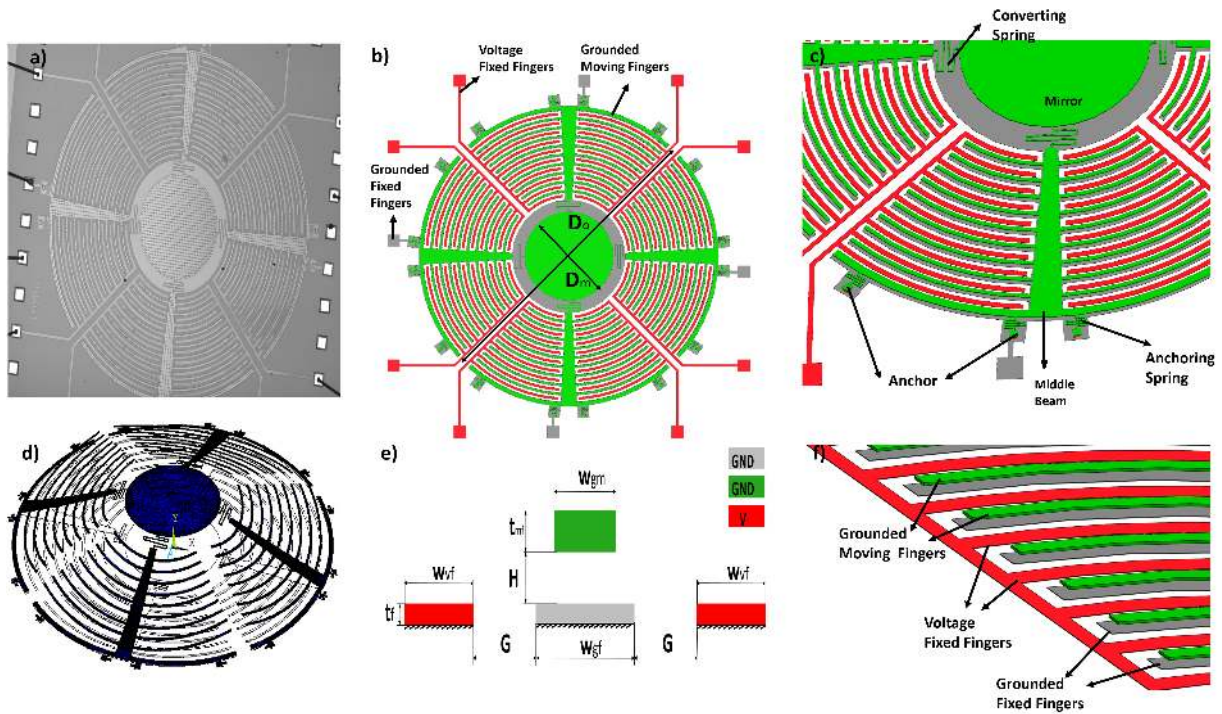
Figure 1: Presented mirror model. (**a**) Microscope image of whole device. (**b**) Top view of 3D model. (**c**) Isometric view of the 3D Model. (**d**) The first mode shape of the system obtained from ANSYS. (**e**) A unit cell of the repulsive actuator configuration. The dimensions are given in Table 1. (**f**) Closer view of the finger configuration in the 3D model.
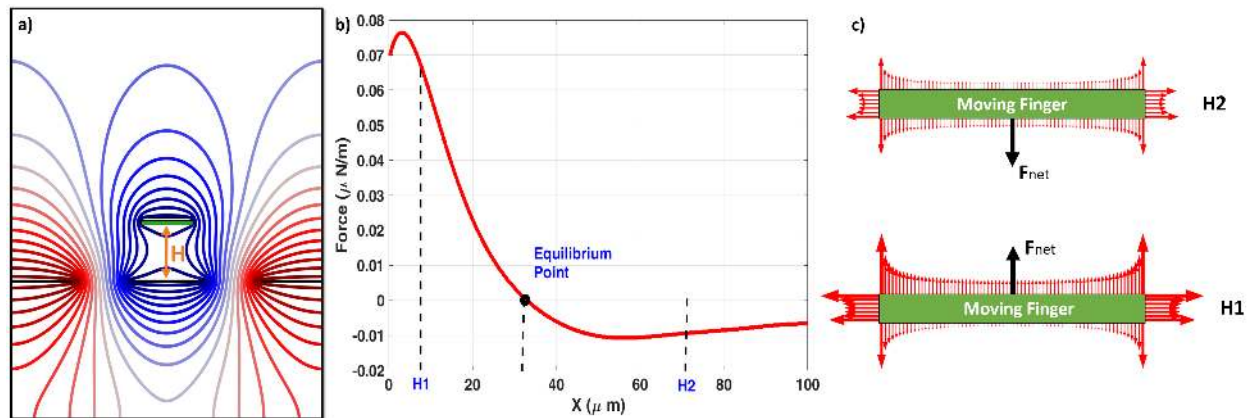

Figure 2: Finite Element Simulation using COMSOL package including (a) Electric field contours, (b) Force profile for the unit cell as the vertical gap H varies at $V = 1\ V$, (c) Electrostatic force distribution on the moving finger at the vertical distance of H_2 (top figure) and H_1 (bottom figure). For the bottom figure, the net force on the moving finger is upward (repulsive). For the top figure, the net force is downward (attractive).

4

Parameter	Symbol	Value	Unit
Actuator mass	m	1.3647×10^{-8}	kg
Actuator outer diameter	D_o	3370	μm
Mirror diameter	D_m	1000	μm
Moving finger width	W_{gm}	20.5	μm
Ground fixed finger width	W_{gf}	32.5	μm
Voltage fixed finger width	W_{vf}	28	μm
Mirror thickness	t_m	2	μm
Moving finger thickness	t_{mf}	2	μm
Ground fixed finger thickness	t_f	0.5	μm
Voltage fixed finger thickness	t_f	0.5	μm
Initial gap	H	0.75	μm
Gap between fixed fingers	G	20.75	μm

Table 1: Dimensions for the MEMS mirror in Figure 1.

This section reports the static and dynamic measurements of the motion of the mirror.

3.1. Static Measurement Setup and Results

We used a WYKO NT 1100 optical profiler to measure the displacement of the mirror center while applying a DC voltage. The optical profiler provides 3D surface profiles of the mirror and the actuators. For our circular finger arrangements, the static displacement curve is presented in Figure 3. The figure indicates that the mirror is released from the substrate after 30 *V*, and it becomes almost stationary beyond 90 *V*. The release voltage depends on the humidity level as the cause of the stiction is the adhesion (capillary) force between substrate and mirror plate [48]. At DC voltages below a threshold voltage (30 *V*), the spring force of the actuators and the generated repulsive force cannot overcome the adhesion force on the mirror, and the mirror stays stationary. At the threshold voltage, the adhesion force gets smaller than the two other forces and the mirror releases from the substrate. The increase in the repulsive force because of increased DC voltage, moves the mirror to higher positions until the position does not increase significantly because of the weak electrostatic force at large gaps around $43\mu m$.

3.2. Dynamic Measurement Setup and Results

The experimental setup for the dynamic tests consists of a data acquisition system and a Laser Doppler Vibrometer (MSA-500). The schematic of experimental setup is depicted in Figure 4. The setup is used to characterize the dynamic behavior of the MEMS mirror under various excitation levels. The displacement decoder of the vibrometer sends an analog input into the DAQ. The data acquisition is NI-6251 (DAQ) from National Instruments connected to a LabVIEW software. The DAQ output passes through a voltage amplifier. An amplified sinusoidal voltage signal goes into the device placed in a vacuum chamber. Simultaneously, the data from the DAQ is entered into the computer and is post-processed to obtain time history and frequency response curves.

To determine the linear natural frequency of the system, we obtain the response at relatively high damping (with a vacuum pressure of 120 mTorr) and low AC excitation ($V_{AC} = 1$ *V*). The
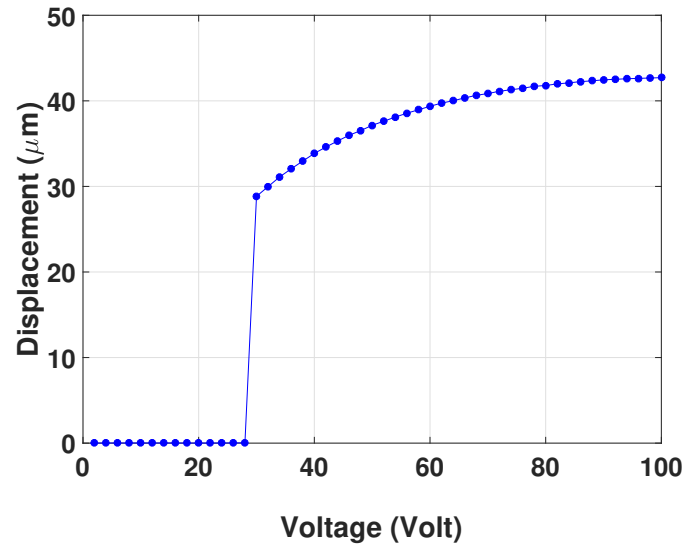
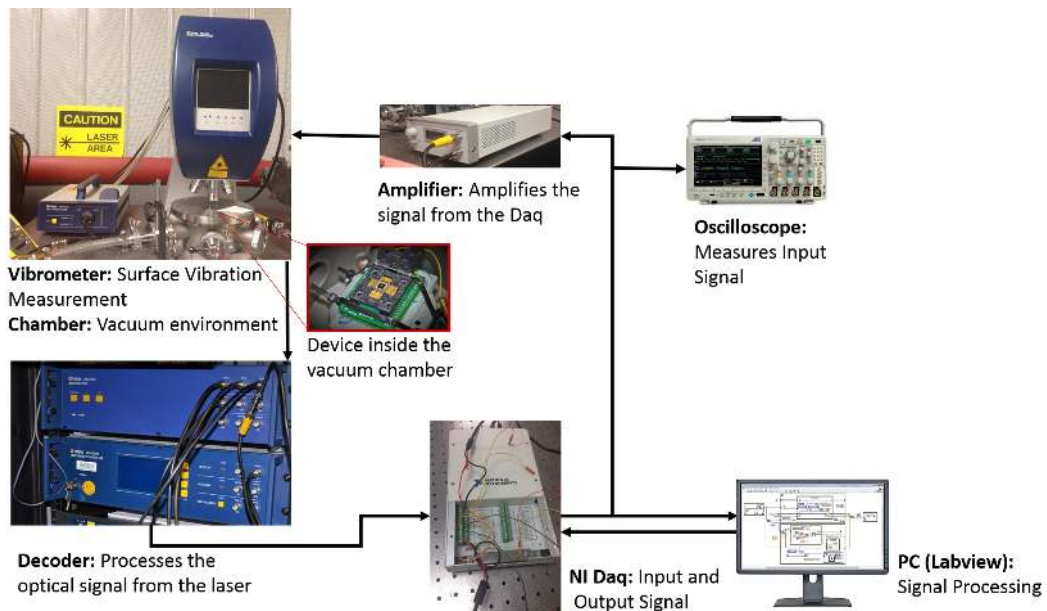Figure 3: Static deflection versus DC Voltage.

Figure 4: Experimental setup with doppler vibrometer

results, shown in Figure 5, reveal a linear increase in the natural frequency as DC voltages increase. This indicates a hardening effect of repulsive force on the linear natural frequency.

To examine the nonlinear response, we decrease the pressure from 120 mTorr to 35 mTorr and record the frequency response curves at different DC voltages keeping the AC voltage constant at 1 *V*, see Figure 6. Results indicate that increasing the DC voltage increases the maximum amplitude at resonance up to a certain voltage (above 50 *V*) and drops at 60 *V*. This fact can be
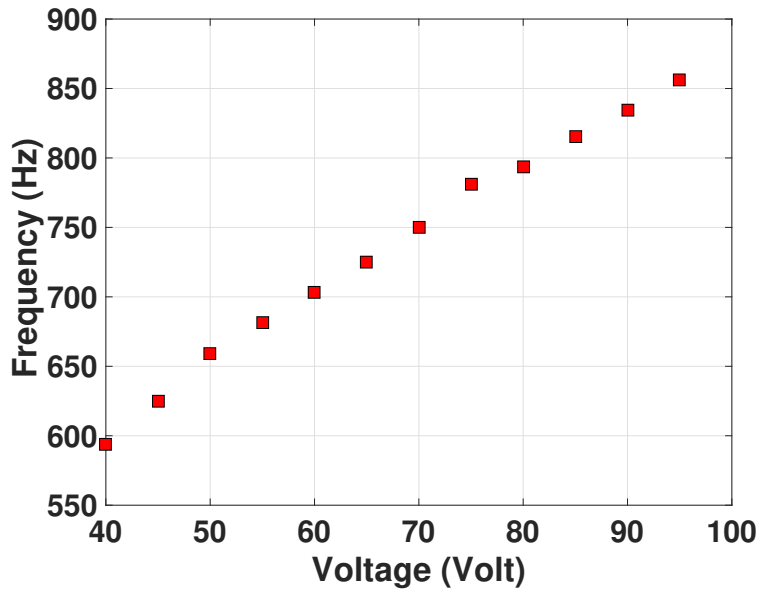
Figure 5: Linear natural frequency obtained for different DC loads at 120 mTorr. Red squares indicate measured values.

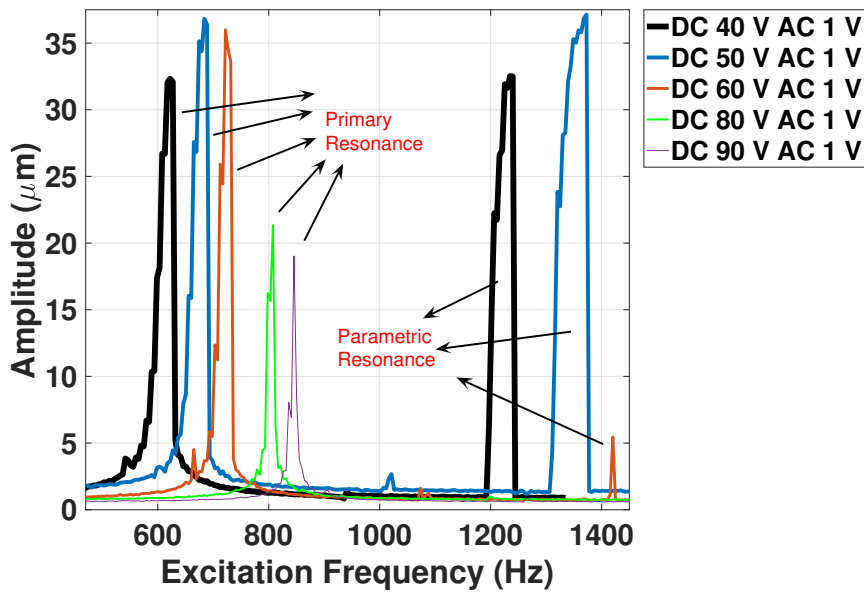Figure 6: Experimental frequency curves as DC voltage varies from 40 *V* to 90 *V* at AC voltage is 1 *V* at 35 mTorr.

explained in corresponding to Figure 3 where at 60 *V*, the slope of the static deflection decreases significantly. In other words, for voltages above 60 *V*, the electrostatic field weakens and the mechanical restoring force dominates (stiffening effect) that causes the drop in the primary resonance

amplitudes. The weak electrostatic field and small amplitudes beyond 60 *V* then suppress the parametric resonance response at twice the natural frequency. This fact can be explained by the reduction of the amplitude term, *u*, and its powers in Equation (14) (described in Section 4.3) that leads to the disappearance of parametric excitation.

Because of our interest in parametric resonance, we conducted our experiments in the low DC voltage range. At low DC excitation levels, the structural nonlinearity is not dominant, and we can observe large parametric resonances at the subharmonic resonance location (twice the natural frequency). These experimental results show that the largest amplitude occurs near the excitation frequency of $2\omega_e/n$ where ω_e is the electromechanical natural frequency of the mirror and $n \geq 1$, i.e. $n = 1$ for the first principal parametric resonance [38, 39, 49, 50]. The time modulated parameters (i.e. linear and cubic stiffness), and low damping are given as the sources of this type of behavior [39, 51, 52]. The source for modulating the electromechanical stiffness is the fringing electric field with time-varying voltage components [42, 53, 54]. In our case the fringe field effect is dominant, which causes large parametric resonances. The oscillations are more pronounced because the pull-in is no longer a limitation. We develop a lumped model to simulate the parametric resonance response as will be described in Section 4.
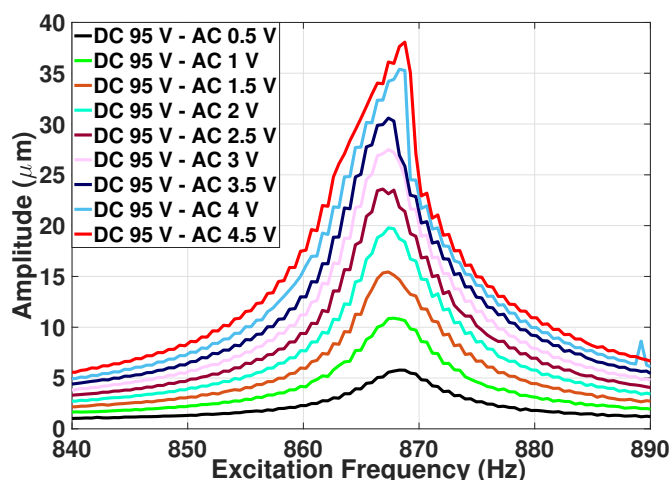

Figure 7: Experimental frequency response curve when DC is 95 V and AC varies from 0.5 to 4.5 V. The pressure of the vacuum chamber is 35 mTorr for this case.

To investigate the effect of AC excitations on the nonlinear responses, we test the mirror at two DC voltages. First, we test the mirror at a high DC voltage of 95 *V* and a low pressure of 35 mTorr. In Figure 7 we present experimental frequency curves for the primary resonance. This figure indicates softening and hardening behavior. It is deduced that at low AC loads, softening behavior is dominant. The presence of the softening behavior is because of the fringing field electrostatic force that will be determined in Section 4.1. The electrostatic force contains a quadratic term (right hand side of Equation (4)) that causes frequency softening. As the AC voltage increases, the response becomes larger and softening behavior turns to hardening. The hardening behavior gets dominant as larger deflections increase the tensile axial stresses. This increase stiffens the structure and is called the midplane stretching effect [55]. The stretching effect appears as a positive cubic
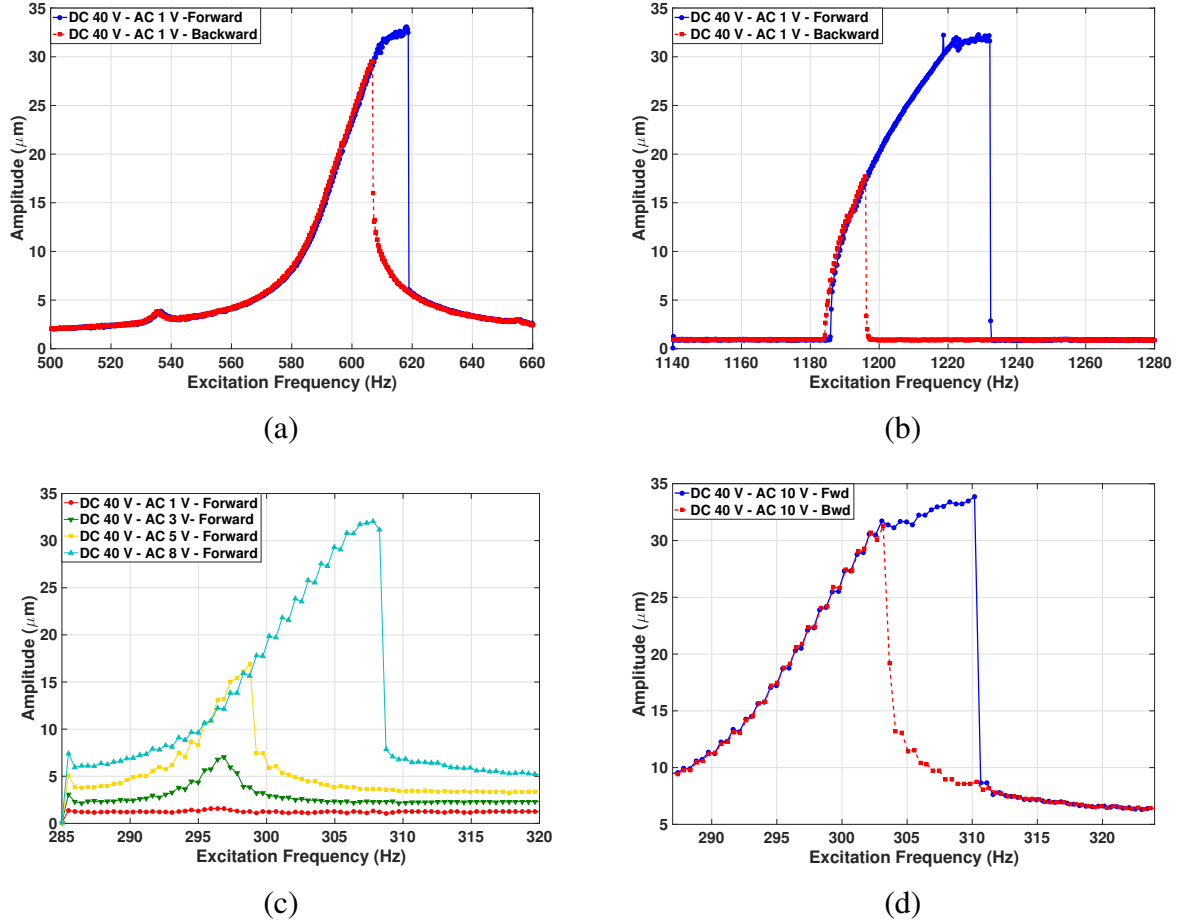
Figure 8: Experimental forward and backward frequency curves when DC load is 40 V at 35 mTorr around (**a**) primary resonance at $V_{AC} = 1$ V. (**b**) Principal parametric resonance at $V_{AC} = 1$ V. (**c**) Superharmonic resonance as AC voltage varies. (**d**) Superharmonic resonance growth at large AC excitation of 10 V.

term in the left-hand side of Equation (4) that dominates the negative cubic term of the electrostatic force. Most of the electrostatically actuated MEMS devices experience softening type of behavior because of a negative quadratic stiffness term. Allowing large deformations (because of pull-in elimination) is a unique property of repulsive force actuation that grows the mid-plane stretching effect in the structure and causes nonlinear frequency hardening. This growing stiffness at high DC voltages prevents the appearance of parametric resonance as seen in Figure 6.

Next, we investigate the response at low DC voltage (when the equivalent stiffness of the actuator is lower) and report a wide range of nonlinear characteristics. Figure 8 presents the frequency response curves near fundamental frequency and secondary resonances at $V_{DC} = 40$ V. Results demonstrate superharmonic resonance of order two and principal parametric resonances at twice the natural frequency. Figure 8a shows that forward and backward sweeps can capture hysteresis. Because this is a hardening-type behavior, the largest amplitude is obtained using forward sweeps. In Figure 8b, we present the frequency response curve of the principal parametric

9

resonance. From the results, we see the same hardening and hysteresis trend as in the primary resonance. Figures 8c and 8d present the effect of AC voltage on superharmonic resonance. The results show that the superharmonic resonance is triggered after a critical AC load and as the amplitude of the AC voltage increases, the hysteresis grows.
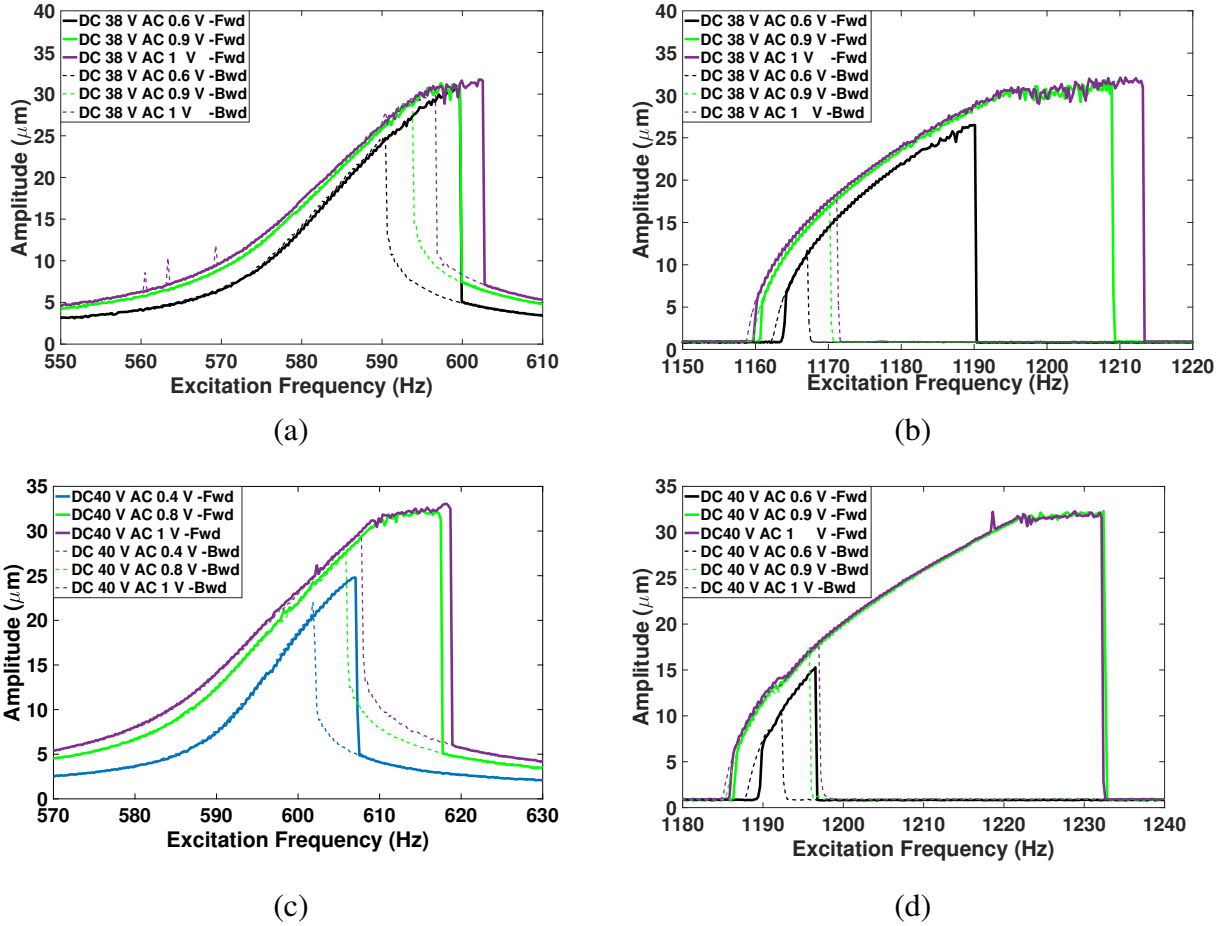

Figure 9: Measured frequency response curve as AC voltage varies for (**a**) fundamental resonance for DC 38 V, (**b**) principal parametric resonance for DC 38 V, (**c**) fundamental resonance for DC 40 V. (**d**) principal parametric resonance for DC 40 V.

To explore how the frequency range for parametric resonance evolves as the voltage increases, we present frequency responses for DC voltages of 38 *V* and 40 *V* as the AC voltage varies from 0.4 *V* to 1 *V*, see Figure 9. Parts (a) and (b) of this figure show the effect of AC load on primary and parametric resonances when the DC voltage is 38 *V* including backward and forward sweeps. For $V_{DC} = 40$ *V* , the fundamental linear resonance occurs at 600 Hz and principal parametric resonance happens at 1.2 kHz at the location of subharmonic resonance of order one-half. It is seen that parametric resonance is as large as the primary resonance. Opposite direction sweeps demonstrate hysteresis, which grows with the increase of AC voltage. The growth of the hysteresis region with the AC voltage is an indication of expansion of transition curves (instability

tongues) for parametric resonance [49]. This huge parametric resonance is a distinct attribute of the repulsive force actuator that enables the effect of electrostatic parametric excitation to thrive because the motion is now not limited to a few microns. Such large amplitudes at high frequency (twice the natural frequency) and low voltage are intriguing features that improve the signal to noise ratio and fast speed in optical measurements.
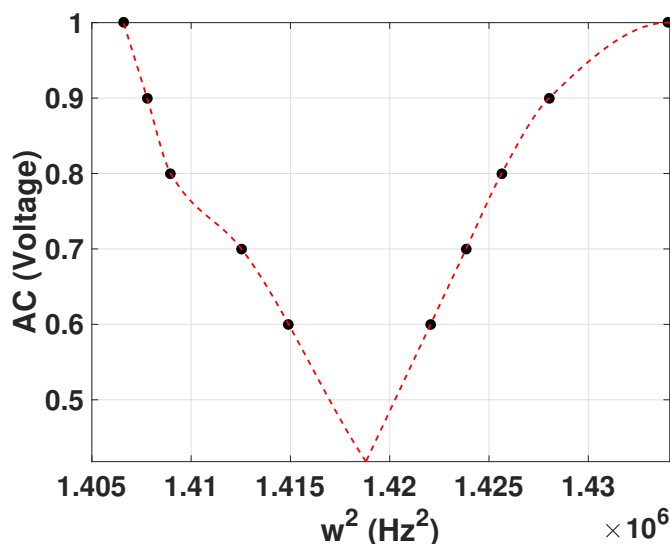

Figure 10: Transition curve of principal parametric resonance for $V_{DC} = 40$ V. Markers indicate measured data and the lines show the data interpolation.

To examine the parameter space where parametric resonance is activated, we mapped the transition curve for the principal parametric resonance of DC 40 V (Figure 10). This curve separates the trivial response from the large bounded parametric resonance inside it. To map the curve, we used the experiments presented in Figure 9d. The curve records the jump frequency of the forward sweep on its left side and the jump frequency of the backward sweep on its right side. It is noticed that if the driving parameters (i.e. AC load and excitation frequency) are within this wedge we can observe the presence of parametric resonance (non-trivial response). If these parameters are outside this wedge, the behavior stays quiescent during the excitation [56]. The transition curve expands by increasing the AC voltage and that proves parametric resonance exists. Also, the presented transition curve shows that, depending on the damping, there is a critical AC voltage input required to see the parametric resonance jumps [53]. For example, in our experiments we could detect parametric resonances for AC voltages above 0.6 V (shown by markers) and we found the intersection of two sides of the curve by interpolation (shown by red line). The AC voltage at this intersection (about 0.42 V) was estimated to be the critical AC load for the appearance of parametric resonance.

4. Mathematical Modeling and System Identification

In this section, we present a lumped parameter model that simulates the nonlinear dynamic nature of the system. Such a simulation can delineate the nonlinear phenomenon observed in the experiment and can be a useful tool to explain the behavior of micro-structures with a repulsive-force mechanism. Modeling the continuous system of our actuator is very sophisticated. One can approximate the micromirror structure in Figure 1 with a single degree of freedom lumped parameter system. We consider a nonlinear lumped parameter oscillator as following:

$$m_f \ddot{\hat{x}} + c_f \dot{\hat{x}} + k_f \hat{x} + \gamma \hat{x}^3 = (V_{dc} + V_{ac} \cos(\Omega \hat{t}))^2 \cdot F(\hat{x}) \tag{1}$$

in which m_f, c_f, k_f and γ are effective mass, damping coefficient, effective stiffness, and cubic stiffness coefficient respectively. The right-hand side represents the electrostatic force. Our lumped system is an equivalent one-degree-of-freedom model that represents the suspension springs consisting of anchoring springs, moving fingers, the middle beam, and the converting spring (Figure 1c). We are studying the first mode that is axis-symmetric. The boundary conditions are the end of anchoring spring, which is a beam clamped to the substrate, and the end of the converting spring, which is a beam attached to the mirror plate. Because the mirror plate acts as a stiff plate, it allows vertical movements, but restricts in-plane displacements. This entails a zero slope and zero shear force at the connection beam to the mirror plate and can be considered as guided boundary condition. We add the nonlinear cubic term based on the mid-plane stretching effect that can be observed for clamped-clamped or clamped-guided beams undergoing large deflection compared to their thickness [55].

By dividing both sides of the Equation (1) by m_f and introducing following non-dimensional parameters

$$x = \frac{\hat{x}}{d}, \qquad t = \frac{\hat{t}}{T}, \qquad T = \frac{1}{\omega_n} \tag{2}$$

we can rewrite it in the following form:

$$\ddot{x} + 2\xi \dot{x} + x + \alpha x^3 = (V_{dc} + V_{ac} \cos(\Omega T t))^2 f(x) \tag{3}$$

where $\omega_n = \sqrt{\frac{k_f}{m_f}}$ is the mechanical natural frequency and $\xi = \frac{c_f}{2\sqrt{m_f k_f}}$ is the damping ratio. Also in this equation, $\alpha = \frac{\gamma d^2}{k}$, $f(x) = \frac{F(xd)}{m_f d \omega_n^2}$ and the right-hand side is the non-dimensional electrostatic force.

4.1. Identification of Electrostatic Force

The electrostatic force can be obtained from numerical methods like a finite element analysis (FEA) or from static experimental data. Here we use the former for two reasons. First, we do not have the Voltage-displacement for DC voltages below 30 V because the mirror is stuck to the substrate. Second, during the static test, the mirror can not go beyond the saturation limit of $44\mu m$ no matter how much voltage we apply. So, again we do not have any Voltage-displacement data

that could give us force-displacement information for displacements larger than 44(μm). Therefore, if we use static test data, at best, we can get the electrostatic force for $30\mu m < x < 44\mu m$ and that does not cover the entire dynamic range of the devices including transient and steady-state regions. To obtain the electrostatic force from FEA, we have used the force profile obtained for a simplified 2D model of the unit cell of the actuator (Figure 2 c). This simplification assumes the moving fingers are rigid and neglects their deformation relative to the middle beams (Figure 1). As we see later, this leads to an overestimation in static simulations, but avoids a time-consuming and complicated simulation of the 3D model.

Using the electrostatic force profile for the 2D model of the actuator unit cell, we obtain an equivalent electrostatic force for the lumped-parameter model as described below. The schematic of the mirror and one set of actuators consisting of movable fingers (beams) is shown in Figure 11. We start from beam 1 and repeat the process for other beams. The cross section of a beam with other electrodes underneath is shown in Figure 1 e and the corresponding the electrostatic force per unit length at 1 V is shown in Figure 2 c. Because of the curved geometry of the beams, each point of a beam experiences different vertical displacement as the mirror lifts (Figure 11). For example, in Figure 11, points B and C are on same beam, but they experience different displacements. In our calculation, the average of displacement at the beginning and end of the beam is considered as the displacement for the beam. Then, multiplying the force by the beam length yields the total force on the beam. Performing this process for each beam and adding force profiles together we can get the force profile as a function of the mirror displacement ($F(\hat{x})$). To get the non-dimensional electrostatic force ($f(x) = \dfrac{F(\hat{x})}{m_f d\omega_n^2}$), we have to estimate the expression of $m_f\omega_n^2$. m_f is the effective mass of the structure considering the contribution of each part in the kinetic energy of the system, which is difficult to obtain. As an estimate, we consider the total mass of the structure (m) as the equivalent mass given in Table 1. ω_n is the mechanical natural frequency, taken from the finite element analysis of the 3D model of the mechanical structure. The nondimensional electrostatic force profile identified for the lumped parameter model is shown in Figure 12.

To examine the accuracy of the identified electrostatic force, we compare the static response obtained from this force profile with the experimental results. Inserting this force profile into Equation (3) and setting the derivatives to zero, we can solve for the static solution and compare it to the static measurements, see Figure 13. It is clear that the force calculated from the 2D FEM model predicts a larger static solution than the experimental results. This discrepancy happens because the model neglects beam deformations relative to their base. In the physical structure, the tips of the beams will be above their base, which causes the tips to experience lower electrostatic force compared to their base. The assumption of a rigid beam leads to an overestimation of the calculated electrostatic force and the static vertical position. However, even with such a simplified lumped parameter force profile, the dynamical response results are promising as will be presented in Subsection 4.3.

Using a 9th order polynomial fit for the force profile of Figure 12, Equation (3) can be rewritten as following.

$$\ddot{x} + 2\xi\dot{x} + x + \alpha x^3 = (V_{dc} + V_{ac}\cos(\frac{\Omega t}{\omega_n}))^2 \sum_{i=0}^{9}(A_i x^i) \qquad (4)$$
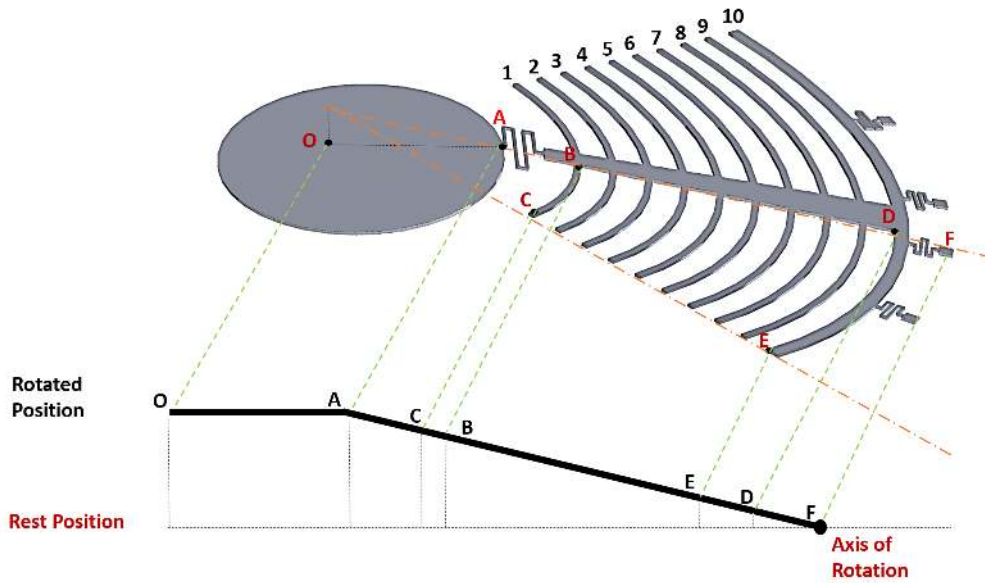
13

Figure 11: Schematic of the mirror and beams in one set of actuators once the mirror lifts
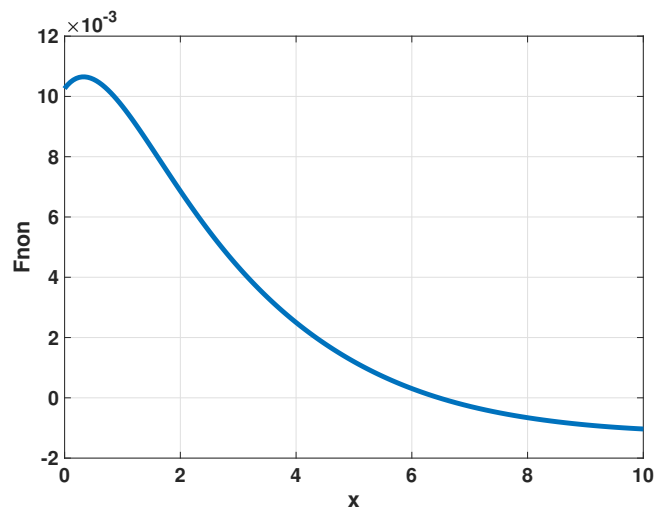
Figure 12: The polynomial fit of the identified electrostatic force at 1 V Volt as the gap varies. This force profile presents the equivalent electrostatic force of the lumped model. The force and the gap are non-dimensional.

where A_i are given in Table 2. Note that electrostatic force, once brought to the left side of the equation, will have a positive quadratic stiffness and a negative cubic stiffness. These nonlinear terms cause frequency softening, which at large deflections evolves to frequency hardening because of the mid-plane stretching effect (positive cubic term on the left side). This is analogous to Figure 7.

Parameter	Symbol	Value
Length used to nondimensionalize	d	$10\ \mu m$
Mechanical Natural Frequency	ω_n	$2\pi \times 300\ rad/s$
Nonlinear spring	α	0.009
Damping ratio	ξ_0	0.0001
Damping ratio	$\xi_1, V_{dc} = 50$ V	0.04
Damping ratio	$\xi_1, V_{dc} = 40$ V	0.06
Non-dimensional Force Constant	A_0	0.0103
Non-dimensional Force Constant	A_1	0.0025
Non-dimensional Force Constant	A_2	-0.0048
Non-dimensional Force Constant	A_3	0.0022
Non-dimensional Force Constant	A_4	-5.4506×10^{-4}
Non-dimensional Force Constant	A_5	8.7048×10^{-5}
Non-dimensional Force Constant	A_6	-8.9464×10^{-6}
Non-dimensional Force Constant	A_7	5.7305×10^{-7}
Non-dimensional Force Constant	A_8	-2.0809×10^{-8}
Non-dimensional Force Constant	A_9	3.2713×10^{-10}

Table 2: Parameters used for mathematical modelling.

4.2. Stiffness and damping Identification

In this section, we determine linear and nonlinear stiffness terms from dynamic test results. First, we construct the Jacobian matrix for the undamped form of Equation (4) at the stable equilibrium point (x_0):

$$A = \begin{bmatrix} 0 & 1 \\ -1 - 3\alpha x_0^2 + V_{dc}^2 \acute{f}(x_0) & 0 \end{bmatrix} \tag{5}$$

By computing the eigenvalues of this matrix, one can determine the linearized electromechanical natural frequency of the system at the equilibrium point by using its imaginary part:

$$f_e = \frac{\omega_n imag(\lambda)}{2\pi} = \frac{\omega_n}{2\pi}\sqrt{+1 + 3\alpha x_0^2 - V_{dc}^2 \acute{f}(x_0)} \tag{6}$$

The resonant frequency at low AC excitations from the experiment is our best guess for this linearized electromechanical natural frequency, f_e that changes linearly with the applied DC voltages (Figure 5). To determine the mechanical natural frequency, ω_n, we use finite element modeling as an initial guess, which yields $\omega_n = 2\pi \times 390 \frac{rad}{s}$. Comparing the results from Equation (6) at two different DC voltages, we found $\omega_n = 2\pi \times 300 \frac{rad}{s}$. This deviation from the finite element results can be explained by imperfect rigid boundaries at the connection of the actuator to the substrate and the initial curvature of the MEMS mirror after fabrication which was not accounted by the FE model. The cubic stiffness, α, is a nonlinearity from tensile axial stress applied to the actuator beams on four sides. As this stress increases with DC voltage, we identify α at different DC voltages to match the experimental results.
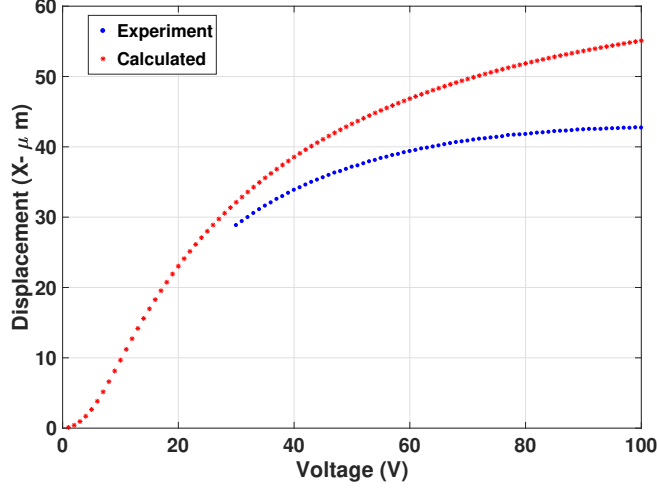
Figure 13: Comparison of the static deflection results from simulations and experiments. For the simulations, the force is calculated from the 2D finite element force profiles.

Vibration of the mirror and its supporting structure in air dissipates energy, which is modeled with a damping coefficient. Because the mirror is tested near the vacuum condition, the continuity of air as a medium is not held and therefore we cannot use continuum based equations like Navier-Stokes to calculate the damping coefficient. Instead damping should be modeled with molecular-regime based approaches. Because of complexity of the mirror structure, simulating the air molecule dynamics and their interaction with the mirror is difficult and computationally expensive. Also during one cycle of vibration the mirror goes through two different energy dissipation mechanisms. For instance, as the mirror is far from the substrate, the interaction between the structure and air molecules is like damping of a moving object in free air. However, as the mirror gets close to the substrate air is trapped between the mirror structure and substrate, and squeeze film damping dominates the energy dissipation. To model this phenomenon, we have used a damping ratio that accounts for the change of damping in one cycle by modulating it with amplitude-gap ratio. This change of damping with amplitude-gap ratio is reported in the [57] for a case of single microbeam. For more explanation on free molecular regime damping one can refer to [58]. The damping ratio and its modulation with amplitude-gap ratio is considered as following.

$$\xi = \xi_0 + \xi_1(\hat{x}/gap) \tag{7}$$

where the gap is the summation of initial gap and static deflection at the DC voltage. The dependence of damping on frequency is not considered in this model. Here, we choose damping ratio coefficients ξ_0 and ξ_1 to match the results with the experimental results as listed in Table 2.

4.3. Simulation Results

Using Equation (4), we can predict the response of the lumped parameter model and investigate its accuracy by comparing it to the experiments. The shooting method (described in the Appendix) is used to obtain the frequency response of the system at two different DC voltages. Damping ratios

16

are identified comparing the simulations against experimental results as listed in Table 2. Figure 14a shows the results for $V_{dc} = 50$ and $V_{ac} = 1$, which is in good agreement with the experimental results. This close agreement validates the lumped parameter model.

To check the model, results are also obtained at $V_{dc} = 40$ V and $V_{ac} = 1$ V (Figure 14b). Comparing theoretical with experimental results, one can notice that the lumped parameter model accurately captures the dynamical amplitude and nonlinear resonance frequency. According to experiments, the maximum response occurs at $f_n = 620(Hz)$, which the model predicts with only a 1.6% error (f_n=630 (Hz)). For the resonance peak amplitude, the model yields almost the same result as the experiment ($34\mu m$). Furthermore, this model can capture the parametric resonance observed in the experiment. The second peak at twice the natural frequency is the principal parametric resonance that shows zero response outside the parametric frequency band. However, there is a difference between predicted and measured amplitudes at the parametric resonance. Authors believe the reason for this lay down in the damping model. The actual damping is far more complicated for the large range of motion the device experiences ($\pm 43\mu m$). This complication becomes worse considering the near vacuum region, where we are at the molecular-damping regime for positions close to the substrate. The simplified damping model also prevents us from having accurate predictions for the resonance bandwidth at very high voltage like 95 V.

In addition, the discrepancy of the bandwidth between simulations and experiments stems from simplifications made to model the whole complicated structures with a simple lumped model. In reality, there are fabrication imperfections and non-ideal boundary conditions which affect the results and are not considered here. Also, the electrostatic force is identified for the lumped model which again is not equal to the actual electrostatic force exerted on the micro structure and that affects the frequency bandwidth.
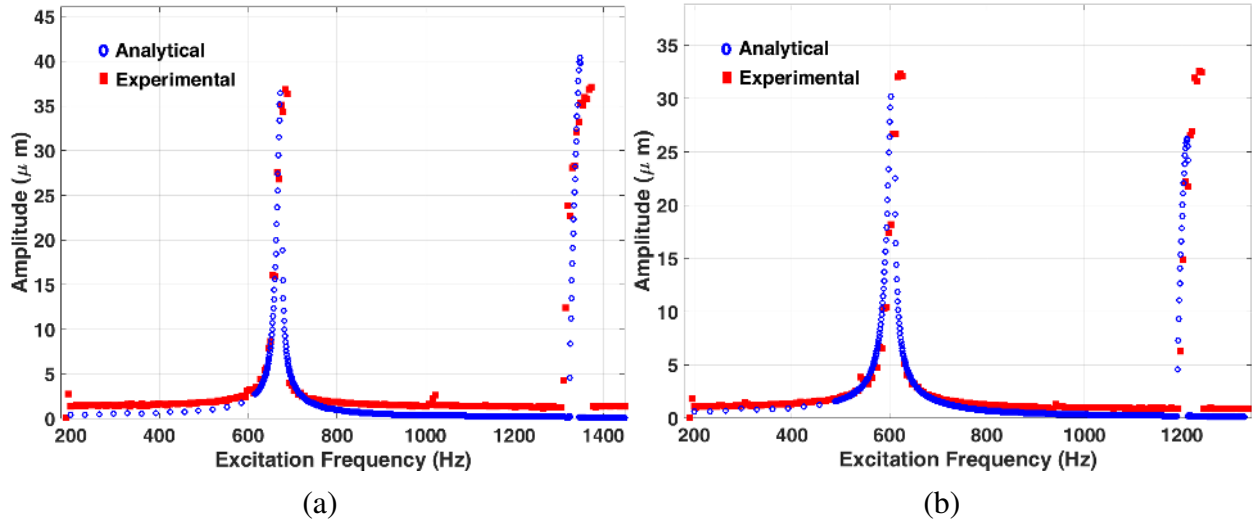

Figure 14: Comparison of simulated and measured frequency responses at (a) $V_{dc} = 50$ V and $V_{ac} = 1$ V, (b) $V_{dc} = 40$ V and $V_{ac} = 1$ V.

The reason for the appearance of parametric resonance will be explained by manipulation of Equation (4) to make it in the form of generalization of Mathieu equation. By expanding the

17

excitation term in Equation (4) one can write

$$\ddot{x} + 2\xi\dot{x} + x + \alpha x^3 = [\tilde{V}_{dc}^2 + \frac{1}{2}V_{ac}^2 Cos(\frac{2\Omega}{\omega_n}t) + 2V_{dc}V_{ac}Cos(\frac{\Omega t}{\omega_n})]\sum_{i=0}^{9}(A_i x^i) \tag{8}$$

where

$$\tilde{V}_{dc} = V_{DC}^2 + \frac{V_{ac}^2}{2} \tag{9}$$

At low AC voltages, we can ignore V_{ac} component ($V_{dc} \gg V_{ac}$). Using the following change of variables

$$x = x_0 + u, \ \tau = \frac{\Omega t}{2\omega_n} \tag{10}$$

where x_0 and u are static and dynamic part of the solution. Ignoring the quartic and higher order terms, we can rewrite Equation (8) in the form of a forced generalization of Mathieu equation up to the third term.

$$\ddot{u} + 2\mu\dot{u} + (\delta_1 + f_1 cos(2\tau))u + (\delta_2 + f_2 cos(2\tau))u^2 + (\delta_3 + f_3 cos(2\tau))u^3 = f_0 cos(2\tau) \tag{11}$$

Its difference with conventional Mathieu equation is that here linear and nonlinear stiffness terms vary with time, while Mathieu equation only contains a time varying linear stiffness. Examples of these generalized Mathieu equation can be found in [52]. In Equation (11), δ_i and f_i are given in the appendix and

$$\mu = \frac{2\xi\omega_n}{\Omega} \tag{12}$$

Equation (11) analytically proves the presence of the principle parametric resonance. Both direct and parametric excitation terms are present in this equation that can explain some observations. From experiments, one notices the characteristic of parametric resonance at twice the natural frequency (Figure 8b), but not at resonance (Figure 8a). That means the response outside the hysteresis region is zero for the former and is nonzero for the latter. This implies that the direct excitation controls the resonance, while the parametric excitation dominates at the twice the resonance. This leads to the appearance of principal parametric resonance and not the fundamental parametric resonance.

5. Conclusion

To summarize, we investigated the nonlinear nature of repulsive force actuators. We presented a lumped parameter model of system that agreed well with the nonlinear responses observed experimentally. We report linear frequency stiffening as a characteristic of repulsive force actuators opposite to parallel-plate actuators, which show linear frequency decreases with increased DC voltages. The repulsive force contains negative cubic and quadratic stiffness terms that cause nonlinear frequency softening; however, they are dominated by the nonlinearity of the large deflection of the structure that causes frequency hardening. Such prominent frequency hardening responses have been rare for parallel plate actuators as their motion is limited to the capacitor gap.

18

Among all nonlinear attributes, the repulsive force actuator shows significant parametric resonance at twice the natural frequency with an amplitude as large as the primary resonance. By manipulating of the governing equation, we have shown the parametric excitation is inherent in the system as the linear, quadratic, and cubic stiffness terms are modulated by the time-varying AC voltage. Our mathematical model enables us to simulate the principal parametric resonances that are in a close agreement with the measured responses. This study indicates repulsive force actuators can be used to create large amplitudes at high frequencies (using parametric resonances) to improve speed and resolution (by increasing signal-to-noise ratio) of imaging devices.

Acknowledgment

References

[1] T. Sandner, C. Drabe, H. Schenk, A. Kenda, W. Scherf, Translatory MEMS actuators for optical path length modulation in miniaturized fourier-transform infrared spectrometers, Journal of Micro/Nanolithography, MEMS, and MOEMS 7 (2) (2008) 021006.

[2] J. W. Jeong, M. J. Mandella, G. S. Kino, C. H. Contag, O. Solgaard, 3-d mems scanning system for dual-axis confocal microendoscopy, in: 16th International Conference on Optical MEMS and Nanophotonics, 2011.

[3] L. Liu, E. Wang, X. Zhang, W. Liang, X. Li, H. Xie, Mems-based 3d confocal scanning microendoscope using mems scanners for both lateral and axial scan, Sensors and Actuators A: Physical 215 (2014) 89–95.

[4] Z. Qiu, W. Piyawattanametha, MEMS-Based Medical Endomicroscopes, IEEE Journal of selected topics in quantum electronics 21 (4).

[5] W. Dajia, S. Guohua, L. Zhang, C. Dongmei, Y. Jun, F. Tianquan, Design of optical coherence tomography probe using a 2-axis mems scanning mirror, in: Proc. of SPIE Vol, Vol. 7284, 2009, pp. 72840Y–1.

[6] T. Xie, H. Xie, G. Fedder, Y. Pan, Endoscopic optical coherence tomography with new mems mirror, Electronics Letters 39 (21) (2003) 1.

[7] J. Dunayevsky, D. M. Marom, Mems spatial light modulator for phase and amplitude modulation of spectrally dispersed light, Journal of Microelectromechanical Systems 22 (5) (2013) 1213–1221.

[8] M. Watanabe, Quality recovery method of interference patterns generated from faulty mems spatial light modulators, Journal of Lightwave Technology 34 (3) (2016) 910–917.

[9] E. H. Yang, K. Shcheglov, S. Trolier McKinstry, Concept, modeling, and fabrication techniques for large-stroke piezoelectric unimorph deformable mirrors, in: Micromachining and Microfabrication, International Society for Optics and Photonics, 2003, pp. 271–278.

[10] T. Sandner, T. Grasshoff, H. Schenk, A. Kenda, Out-of-plane translatory MEMS actuator with extraordinary large stroke for optical path length modulation, in: SPIE MOEMS-MEMS, International Society for Optics and Photonics, 2011, pp. 79300I–79300I.

[11] P. Y. Lin, H. T. Hsieh, G. D. J. Su, Design and fabrication of a large-stroke MEMS deformable mirror for wavefront control, Journal of Optics 13 (5) (2011) 055404.

[12] S. Nam, S. Park, S. Yun, B. Park, S. Park, K. U. Kyung, Structure modulated electrostatic deformable mirror for focus and geometry control, Optics Express 24 (1) (2016) 55–66.

[13] J. L. Wang, T. Y. Chen, Y. H. Chien, G. D. J. Su, Miniature optical autofocus camera by micromachined fluoropolymer deformable mirror, Opt. Express 17 (8) (2009) 6268–6274.

[14] D. J. Dagel, W. D. Cowan, O. B. Spahn, G. D. Grossetete, A. J. Grine, M. J. Shaw, P. J. Resnick, B. Jokiel, Large-stroke mems deformable mirrors for adaptive optics, Journal of Microelectromechanical Systems 15 (3) (2006) 572–583.

[15] V. Milanovic, S. Kwon, L. P. Lee, High aspect ratio micromirrors with large static rotation and piston actuation, IEEE Photonics Technology Letters 16 (8) (2004) 1891–1893.

[16] S. He, R. Ben Mrad, Development of a novel translation micromirror for adaptive optics, in: Photonics Technologies for Robotics, Automation, and Manufacturing, International Society for Optics and Photonics, 2003, pp. 154–161.

[17] T. Sandner, T. Grasshoff, H. Schenk, Translatory MEMS actuator with extraordinary large stroke for optical path length modulation, in: 2010 International Conference on Optical MEMS and Nanophotonics, IEEE, 2010, pp. 25–26.

[18] T. Y. Chen, C. W. E. Chiu, G. D. J. Su, A large stroke MEMS deformable mirror fabricated by low-stress fluoropolymer membrane, IEEE Photonics Technology Letters 20 (10) (2008) 830–832.

[19] R. Nadal-Guardia, A. Deh, R. Aigner, L. M. Castaer, Current drive methods to extend the range of travel of electrostatic microactuators beyond the voltage pull-in point, Journal of Microelectromechanical Systems 11 (3).

[20] J. I. Seeger, B. E. Boser, Charge control of parallel plate electrostatic actuators and the tip-in instability, Journal of Microelectromechanical Systems 12 (5).

[21] E. S. Hung, S. D. Senturia, Extending the travel range of analog tuned electrostatic actuators, Journal of Microelectromechanical Systems 8 (4).

[22] E. K. Chan, R. W. Dutton, Electrostatic micromechanical actuator with extended range of travel, Journal of Microelectromechanical Systems 9 (3).

[23] M. A. Rosa, D. D. Bruyker, A. R. V. Olkel, E. Peeters, J. Dunec, A novel external electrode configuration for the electrostatic actuation of mems based devices, Journal of Micromechanics and Microengineering 14.

[24] D. Y. Qiao, W. Z. Yuan, X. Y. Li, A two-beam method for extending the working range of electrostatic parallel-plate micro-actuators, Journal of Electrostatics 65.

[25] J. C. Chiou, Y. J. Lin, A novel large displacement electrostatic actuator: pre-stress comb-drive actuator, Journal of Micromechanics and Microengineering 15.

[26] G. Zhou, P. Dowd, Tilted folded-beam suspension for extending the stable travel range of comb-drive actuators, Journal of Micromechanics and Microengineering 13.

[27] S. He, R. Ben Mrad, Large-stroke microelectrostatic actuators for vertical translation of micromirrors used in adaptive optics, IEEE Transactions on Industrial Electronics 52 (4) (2005) 974–983.

[28] W. C. Tang, M. G. Lim, R. T. Howe, Electrostatic comb drive levitation and control method, Journal of Microelectromechanical systems 1 (4) (1992) 170–178.

[29] K. B. Lee, Y. H. Cho, Laterally driven electrostatic repulsive-force microactuators using asymmetric field distribution, Microelectromechanical Systems, Journal of 10 (1) (2001) 128–136.

[30] S. He, R. Ben Mrad, J. Chong, Repulsive force out-of-plane large stroke translation micro electrostatic actuator, Journal of Micromechanics and Microengineering 21 (7) (2011) 075002.

[31] S. He, R. Ben Mrad, Design, modeling, and demonstration of a MEMS repulsive-force out-of-plane electrostatic micro actuator, Journal of Microelectromechanical Systems 17 (3) (2008) 532–547.

[32] F. Alsaleem, M. I. Younis, H. Ouakad, On the nonlinear resonances and dynamic pull-in of electrostatically actuated resonators, Journal of Micromechanics and Microengineering 19 (2009) 045013(1–14).

[33] E. M. Abdel Rahman, A. H. Nayfeh, Secondary resonances of electrically actuated resonant microsensors, Journal of Micromechanics and Microengineering 13 (2003) 1–11.

[34] M. I. Younis, A. H. Nayfeh, A study of the nonlinear response of a resonant microbeam to an electric actuation, Nonlinear Dynamics 31 (2003) 91–117.

[35] M. Ozdogan, S. Towfighian, Nonlinear dynamic behavior of a bi-axial torsional MEMS mirror with sidewall electrodes, Micromachines 7 (3) (2016) 42.

[36] Y. K. Hong, R. R. Syms, Dynamic response modeling of MEMS micromirror corner cube reflectors with angular vertical combdrives, Journal of Lightwave Technology 25 (2) (2007) 472–480.

[37] W. Shahid, Z. Qiu, X. Duan, H. Li, T. D. Wang, K. R. Oldham, Modeling and simulation of a parametrically resonant micromirror with duty-cycled excitation, Journal of Microelectromechanical Systems 23 (6) (2014) 1440–1453.

[38] D. Rugar, P. Grütter, Mechanical parametric amplification and thermomechanical noise squeezing, Physical Review Letters 67 (6) (1991) 699.

[39] K. L. Turner, S. A. Miller, P. G. Hartwell, N. C. MacDonald, S. H. Strogatz, S. G. Adams, Five parametric resonances in a microelectromechanical system, Nature 396 (6707) (1998) 149–152.

[40] J. J. Garcia Ripoll, V. M. Perez Garcia, P. Torres, Extended parametric resonances in nonlinear schrödinger systems, Physical review letters 83 (9) (1999) 1715.

[41] J. F. Rhoads, S. W. Shaw, K. L. Turner, J. Moehlis, B. E. DeMartini, W. Zhang, Generalized parametric resonance in electrostatically actuated microelectromechanical oscillators, Journal of Sound and Vibration 296 (4) (2006) 797–829.

[42] Y. Linzon, B. Ilic, S. Lulinsky, S. Krylov, Efficient parametric excitation of silicon-on-insulator microcantilever beams by fringing electrostatic fields, Journal of Applied Physics 113 (16) (2013) 163508.

[43] S. Krylov, Y. Gerson, T. Nachmias, U. Keren, Excitation of large-amplitude parametric resonance by the mechanical stiffness modulation of a microstructure, Journal of Micromechanics and Microengineering 20 (1) (2009) 015041.

[44] C. Ataman, O. Kaya, H. Urey, Analysis of parametric resonances in comb driven microscanners, in: Photonics Europe, International Society for Optics and Photonics, 2004, pp. 128–136.

[45] H. Ra, W. Piyawattanametha, Y. Taguchi, D. Lee, M. J. Mandella, O. Solgaard, Two dimensional mems scanner for dual-axes confocal microscopy, Journal of Microelectromechanical systems 16 (4) (2007) 969–976.

[46] Z. Qiu, Z. Liu, X. Duan, S. Khondee, B. Joshi, M. J. Mandella, K. Oldham, K. Kurabayashi, T. D. Wang, Targeted vertical cross-sectional imaging with handheld near-infrared dual axes confocal fluorescence endomicroscope, Biomed. Opt. Express 4 (2) (2013) 322–330.

[47] A. Cowen, G. Hames, D. Monk, S. Wilcenski, B. Hardy, Soimumps design handbook, MEMSCAP Inc (2011) 2002–2011.

[48] N. Tas, T. Sonnenberg, H. Jansen, R. Legtenberg, M. Elwenspoek, Stiction in surface micromachining, Journal of Micromechanics and Microengineering 6 (4) (1996) 385.

[49] A. H. Nayfeh, D. T. Mook, Nonlinear oscillations, John Wiley & Sons, 2008.

[50] A. Ramini, N. Alcheikh, S. Ilyas, M. Younis, Efficient primary and parametric resonance excitation of bistable resonators, AIP Advances 6 (9) (2016) 095307.

[51] W. Zhang, R. Baskaran, K. L. Turner, Effect of cubic nonlinearity on auto-parametrically amplified resonant MEMS mass sensor, Sensors and Actuators A: Physical 102 (12) (2002) 139 – 150.

[52] B. E. DeMartini, J. F. Rhoads, K. L. Turner, S. W. Shaw, J. Moehlis, Linear and nonlinear tuning of parametrically excited mems oscillators, Journal of Microelectromechanical Systems 16 (2) (2007) 310–318.

[53] J. F. Rhoads, S. W. Shaw, K. L. Turner, R. Baskaran, Tunable microelectromechanical filters that exploit parametric resonance, Journal of Vibration and Acoustics 127 (5) (2005) 423–430.

[54] M. Pallay, S. Towfighian, Parametrically excited electrostatic MEMS cantilever beam with flexible support, Journal of Vibration and Acoustics 139 (2) (2017) 021002.

[55] M. I. Younis, MEMS linear and nonlinear statics and dynamics, Vol. 20, Springer Science & Business Media, 2011.

[56] J. F. Rhoads, C. Guo, G. K. Fedder, Parametrically excited micro and nanosystems, no. 5, Wiley-VCH Verlag GmbH Co. KGaA, 2015.

[57] S. Hutcherson, W. Ye, On the squeeze-film damping of micro-resonators in the free-molecule regime, Journal of Micromechanics and Microengineering 14 (12) (2004) 1726.

[58] H. Sumali, Squeeze-film damping in the free molecular regime: model validation and measurement on a mems, Journal of Micromechanics and Microengineering 17 (11) (2007) 2231.

Appendix A: Shooting Method

To find the dynamic response of the system, Equation (4) is solved using shooting techniques outlined in [55]. First, Equation (4) is rewritten in state-space form.

$$\begin{cases} \dot{x}_1 = x_2 \\ \dot{x}_2 = -2\xi\dot{x}_2 + -x_1 - \alpha x_1^3 + (V_{dc} + V_{ac}Cos(\frac{\Omega t}{\omega_n}))^2 \sum_{i=1}^{9}(A_i x_1^i) \end{cases}$$

21

Then, four new variables are defined to help find the initial conditions to capture the steady-state response.

$$x_3 = \frac{\partial x_1}{\partial \eta_1} \qquad x_4 = \frac{\partial x_1}{\partial \eta_2} \qquad x_5 = \frac{\partial x_2}{\partial \eta_1} \qquad x_6 = \frac{\partial x_2}{\partial \eta_2}$$

where η_1 is the initial displacement and η_2 is the initial velocity. Including the newly defined variables, the state-space equations become:

$$\begin{cases} \dot{x}_1 = x_2 \\ \dot{x}_2 = -2\xi \dot{x}_2 + -x_1 - \alpha x_1^3 + (V_{dc} + V_{ac}Cos(\frac{\Omega t}{\omega_n}))^2 \sum_{i=1}^{9}(A_i x_1^i) \\ \dot{x}_3 = x_5 \\ \dot{x}_4 = x_6 \\ \dot{x}_5 = (-1 - 3\alpha x_1^2 + (V_{dc} + V_{ac}Cos(\frac{\Omega t}{\omega_n}))^2 \sum_{i=1}^{9}(A_i i x_1^{i-1}))x_3 - 2\xi x_5 \\ \dot{x}_6 = (-1 - 3\alpha x_1^2 + (V_{dc} + V_{ac}Cos(\frac{\Omega t}{\omega_n}))^2 \sum_{i=1}^{9}(A_i i x_1^{i-1}))x_4 - 2\xi x_6 \end{cases}$$

They are integrated over one period (T) using ode45 in MATLAB with the initial conditions shown below.

$$x(0) = [\eta_1 \quad \eta_2 \quad 1 \quad 0 \quad 0 \quad 1]$$

To determine the approximate error in the initial conditions, $\partial \eta_i$, the results for x at time T are used in the following equation,

$$\begin{Bmatrix} \partial \eta_1 \\ \partial \eta_2 \end{Bmatrix} = \left[\begin{Bmatrix} x_3(T) & x_4(T) \\ x_5(T) & x_6(T) \end{Bmatrix} - \begin{Bmatrix} 1 & 0 \\ 0 & 1 \end{Bmatrix} \right]^{-1} \begin{Bmatrix} \eta_1 - x_1(T) \\ \eta_2 - x_2(T) \end{Bmatrix}$$

The initial conditions are then corrected with using the approximate error.

$$x = [\eta_1 + \partial \eta_1 \quad \eta_2 + \partial \eta_2 \quad 1 \quad 0 \quad 0 \quad 1]$$

This process is repeated until the errors are sufficiently small and the results for x_1 and x_2 converge. To analyze the stability of the solution, the monodromy matrix is constructed.

$$\begin{bmatrix} x_3(T) & x_4(T) \\ x_5(T) & x_6(T) \end{bmatrix}$$

The eigenvalues of the monodromy matrix (Floquet multipliers) show whether the solution is stable. Floquet multipliers outside the unity circle in the complex plane indicate an unstable solution while inside the unity circle indicate stable solutions [49].

Coefficient of generalization of Mathieu Equation

$$\delta_1 = (\frac{2\omega_n}{\Omega})^2 (1 + 3\alpha x_0^2 - \tilde{V}_{dc}^2 \sum_{i=1}^{9} i A_i x_0^{i-1}) \qquad (13)$$

$$\delta_2 = (\frac{2\omega_n}{\Omega})^2 (3\alpha x_0 - \tilde{V}_{dc}^2 \sum_{i=2}^{9} \frac{i(i-1)}{2} A_i x_0^{i-2}) \qquad (14)$$

$$\delta_3 = (\frac{2\omega_n}{\Omega})^2 (\alpha - \tilde{V}_{dc}^2 \sum_{i=3}^{9} \frac{i(i-1)(i-2)}{6} A_i x_0^{i-3}) \qquad (15)$$

$$f_0 = 2 V_{dc} V_{ac} \sum_{i=0}^{9} A_i x_0^i \qquad (16)$$

$$f_1 = (\frac{2\omega_n}{\Omega})^2 (-2 V_{dc} V_{ac} \sum_{i=1}^{9} i A_i x_0^{i-1}) \qquad (17)$$

$$f_2 = (\frac{2\omega_n}{\Omega})^2 (-2 V_{dc} V_{ac} \sum_{i=2}^{9} \frac{i(i-1)}{2} A_i x_0^{i-2}) \qquad (18)$$

$$f_3 = (\frac{2\omega_n}{\Omega})^2 (-2 V_{dc} V_{ac} \sum_{i=3}^{9} \frac{i(i-1)(i-2)}{6} A_i x_0^{i-3}) \qquad (19)$$